Journal of Alloys and Compounds 509 (2011) 7221–7228

Contents lists available at ScienceDirect

Journal of Alloys and Compounds

journal homepage: www.elsevier.com/locate/jallcom

Microstructure and microhardness evolution of a $Mg_{83}Ni_6Zn_5Y_6$ alloy upon annealing

X.H. Shao [a], Z.Q. Yang [a], J.H. You [b], K.Q. Qiu [b], X.L. Ma [a,*]

[a] Shenyang National Laboratory for Materials Science, Institute of Metal Research, Chinese Academy of Sciences, 72 Wenhua Road, 110016 Shenyang, China
[b] School of Materials Science and Engineering, Shenyang University of Technology, 111 Shenliao West Road, Economic & Technological Development Zone, 110178 Shenyang, China

ARTICLE INFO

Article history:
Received 1 October 2010
Received in revised form 10 April 2011
Accepted 11 April 2011
Available online 20 April 2011

Keywords:
Mg alloy
Microstructure
Microhardness
Long period stacking ordered phase
Intermetallic phase

ABSTRACT

The microstructures and the corresponding microhardness evolution of a $Mg_{83}Ni_6Zn_5Y_6$ (at.%) alloy subjected to a series of heat treatments were investigated. In addition to the 14H long period stacking ordered (LPSO) phase, a diamond-cubic phase with the possible space group of $Fd\bar{3}m$ and lattice parameter of $a = 0.73$ nm were identified in the as-cast alloy. The combination of LPSO thin lamellae and the nanometer-sized cubic phase leads to a relatively high Vickers microhardness of about 116.2 ± 13.7. When annealed at 473 K and 573 K, the above diamond-cubic phase partially transforms to its structural variant, $Fm\bar{3}m$, together with a slight change of lattice parameter ($a = 0.72$ nm). Precipitation of hexagonal Mg_2Ni lath also happens at these moderate annealing temperatures. The remarkable increase of microhardness at this stage is believed to result from the strengthening of precipitates and the resultant coherent interface between the precipitates and their surrounding medium. When annealed at temperatures ranging from 673 K to 773 K, the Mg_2Ni precipitates were dissolved, grain coarsening in the alloy occurred, $Fd\bar{3}m$ phase completely transformed to its $Fm\bar{3}m$ counterpart, and consequently microhardness of the alloy was decreased significantly.

1. Introduction

Magnesium alloys are currently of great interest, as their extraordinary low density, high specific strength, and easy-recycling ability are very attractive for further applications in aeronautics, electronics and other consumer goods. However, the relatively low strength of Mg alloys strongly restricts their potential applications. Recently, a number of Mg alloys containing rare earth (RE) element are found to be optimized by several second phases [1–5] which play a critical role in improving the mechanical performance, such as high creep strength, high strength and corrosion resistance. In Mg–Zn–Y–(Zr) alloys, it is known that the Zn/Y ratios are able to tune the presence of various intermetallic phases including binary Mg–Zn phase, icosahedral (I) phase, $Mg_3Zn_3Y_2$ (W) phase [4], and long period stacking ordered (LPSO) phase [5–9]. As a consequence, mechanical performance of Mg–Zn–Y alloys is strongly associated with Zn/Y ratios [3–9]. In contrast, a Ni/Y ratio in an Mg–Ni–Y system plays a different role from Zn/Y in Mg–Zn–Y alloy. For example, a $Mg_{90.5}Ni_{3.25}Y_{6.25}$ (at.%) alloy exhibits high strength owing to formation an LPSO phase [10], while the $Mg_{83}Ni_{9.5}Y_{7.5}$ alloy was strengthened during annealing by three kinds of precipitate, $Mg_{24}Y_5$, Mg_2Ni, and Ni_2Y_3 [11]. Icosahedral phase was not found in Mg–Ni–RE alloys. To date, little work has been done in quaternary Mg–Ni–Zn–Y alloys, although a quaternary $Mg_{90}(Cu_{0.667}Y_{0.333})_4Zn_6$ alloy is found to exhibit ultimate compressive strength of over 700 MPa and compressive plasticity of as high as 11.7%. Such an attractive performance is proposed to resulted from special eutectic structure (α-Mg + Cu_2Mg + CuMgZn) and refinement of Mg dendrite [12].

The objective of the present study was to explore microstructural characteristics and their effect on mechanical performance in a quaternary Mg–Ni–Zn–Y alloy. We present a spectrum of microstructures and corresponding microhardness in various annealing states, which is expected to provide useful information for optimizing the mechanical properties via heat treatment of new Mg alloys.

2. Experimental procedures

A quaternary alloy with a nominal composition $Mg_{83}Ni_6Zn_5Y_6$ (at.%) was prepared. Firstly, an intermediate alloy Ni–Y ingot was arc-melted in an argon atmosphere. Then high purity Mg (99.99%) and Zn (99.99%) pieces with Ni–Y ingot were melted in an induction furnace to obtain the master alloys $Mg_{83}Ni_6Zn_5Y_6$ (at.%). Finally, the master alloys were remelted in a quartz tube and injected into a copper mould to obtain rods with a diameter of 3 mm. Some samples, which were sealed in quartz tube in an Ar atmosphere in order to avoid Mg alloy oxidation, were annealed in the temperature range of 473–773 K with a constant annealing time of 5 h. Microhardness was measured on an MVK-H300 Vikers hardness testing machine, with a load of 50 g and a loading time of 10 s. The hardness values shown in this study were averaged from at least 20 indentations on each sample.

* Corresponding author. Tel.: +86 24 23971845.
E-mail address: xlma@imr.ac.cn (X.L. Ma).

0925-8388/$ – see front matter © 2011 Elsevier B.V. All rights reserved.
doi:10.1016/j.jallcom.2011.04.067

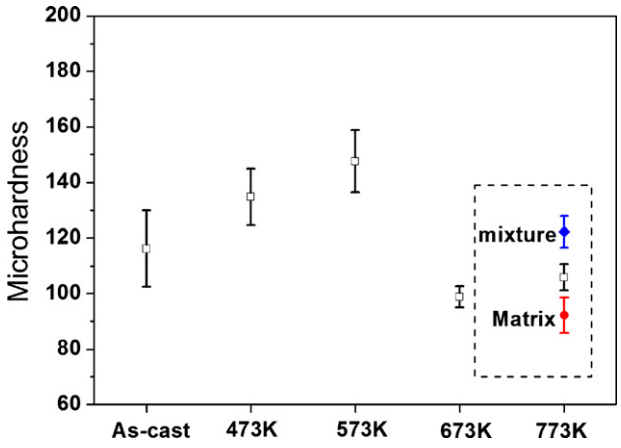

Fig. 1. The variation of microhardness of Mg–Ni–Zn–Y alloy under as-cast state and different annealing temperatures. The matrix and the distinct microstructure in sample S-773 are large enough to be measured independently, and their microhardness are illustrated in the rectangle.

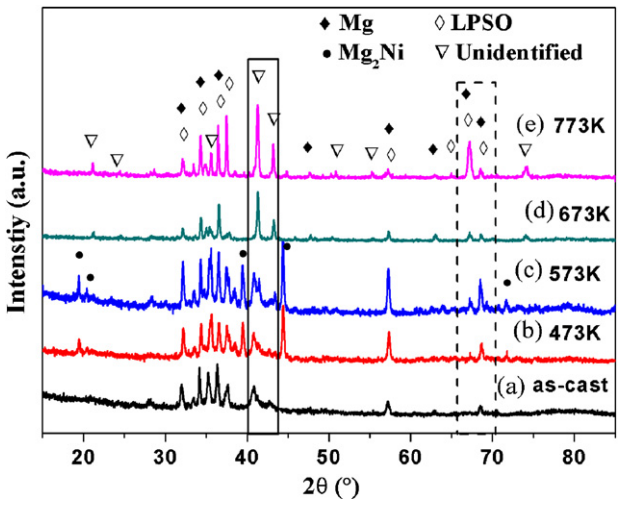

Fig. 2. X-ray diffraction patterns of the Mg–Ni–Zn–Y alloy under as-cast state and different annealing temperatures (473 K, 573 K, 673 K and 773 K). The peaks at $2\theta \approx 40.8^\circ$ and $2\theta \approx 42.7^\circ$ split into two in spectra (b) and (c), marked by a solid rectangle. And there is a reversion of intensity ratio of the peaks $2\theta \approx 67.3^\circ$ and that at $2\theta \approx 68.6^\circ$ in spectra (b and c) and in spectra (d and e), shown by a dashed rectangle.

The phase constitution was analyzed using XRD in a Rigaku D/max 2500-PC diffractometer with Cu *Kα* radiation ($\lambda = 0.154178$ nm), in the 2θ range of 15–80° with a scan rate of 0.02°/step. The microstructures of samples were examined by a scanning electron microscope (SEM: Cambridge S-360 and LEO SUPRA 35-FEG-SEM) and a transmission electron microscope (TEM). Thin foil samples for TEM observation were prepared by conventional ion-milling method. A Tecnai G^2 F30 TEM, which was operated at 300 kV and equipped with an energy-dispersive X-ray (EDX) detector and a high-angle annual dark-field (HAADF) detector, was used for microstructural investigations. For simplicity, samples at as-cast state and annealed at 473 K, 573 K, 673 K and 773 K hereafter are referred to as samples S-cast, S-473, S-573, S-673 and S-773, respectively.

3. Results

3.1. Microhardness evolution

Fig. 1 illustrates the microhardness evolution of the $Mg_{83}Ni_6Zn_5Y_6$ (at.%) alloy upon annealing. The Vikers microhardness of sample S-cast was measured to be 116.2 ± 13.7. The microhardness of samples S-473 and S-573 increased to 134.8 ± 10.2 and 147.6 ± 11.2, respectively. In contrast, the microhardness decreased to 98.9 ± 3.8 after the alloy was annealed at 673 K. In the sample S-773, the second phase was so large that microhardness tests could be performed on it and the matrix separately, which are 121.3 ± 4.5 and 97.7 ± 5.0, respectively. For a comparison with other samples, a weighted average microhardness of 105.9 ± 4.7 was determined for sample S-773, based on the volume fractions of the phase constituents.

3.2. General microstructures of the Mg–Ni–Zn–Y alloy under different states

Fig. 2 shows the XRD spectra taken from the cross section of $Mg_{83}Ni_6Zn_5Y_6$ (at.%) samples with various states. The basic peaks in the spectrum of the as-cast alloy can be indexed as reflections from Mg and LPSO phase, except peaks at 2θ around 40.5° and 42.5°. The XRD patterns of samples S-473 and S-573 (spectra (b) and (c)) are similar to each other, where hexagonal Mg_2Ni phase can be indexed. It is of interest to note that the peaks at $2\theta \approx 40.8^\circ$ and $2\theta \approx 42.7^\circ$ split into two in spectra (b) and (c), marked by a solid rectangle in Fig. 2. Samples S-673 and S-773 display similar XRD spectra, shown in (d) and (e), where it is seen that the intensity of the diffraction peaks from Mg_2Ni phase drops dramatically, and simultaneously some new peaks (denoted by ▽) become obvious, implying an occurrence of phase transformation at high annealing temperature. Furthermore, the intensity ratio of the peak at $2\theta \approx 67.3^\circ$ and that at $2\theta \approx 68.6^\circ$ reversed in spectra (b and c) and in spectra (d and e), marked by a dashed rectangle in Fig. 2.

Fig. 3 shows back scattered electron (BSE)-SEM images of samples S-cast, S-473, S-673 and S-773. Sample S-cast was mainly composed of a ternary eutectic, in which all the phases are distinguished by white, gray and black lamellae due to the difference in elemental concentrations. The homogenous white and gray lamellae (with 1 μm in thickness and several tens microns in length) are stacked alternatively with each other, forming layered structures of various orientations. The layered structures with different orientations may cross each other, as marked by circles in Fig. 3a. EDX measurements in the SEM (Table 1) show that the gray lamellae are richer of Mg, but poorer of Ni, Zn and Y, compared to the white ones. The dark regions, indicated by black arrows in Fig. 3a, about 2 μm in diameter and several microns in length, were composed mainly of Mg. Thus, the phase with dark contrast could be identified as Mg solid solution, and the gray lamellae are LPSO phase [13,14]. The white lamellae (Fig. 3a) are remarkably rich in Ni and Zn, compared with the Mg solid solution and LPSO phase. This might be responsible for the unidentified peaks in spectrum (a) for sample S-cast in Fig. 2.

A great number of light gray plates as denoted by white arrows in Fig. 3b, about 1.5 μm in diameter, are homogenously distributed in sample S-473. This phase mainly consists of Mg (56–62 at.%), Ni (28–34 at.%), which should be Mg_2Ni phase detected by XRD in Fig. 2b. Meanwhile, some small white particles are attached to the Mg_2Ni phase, as shown by black arrows in Fig. 3b. The composition of these particles is a little different from that of the white lamellae in sample S-cast, i.e. the concentration of Mg decreased while that of Ni and Zn increased. The thick dark gray bands in Fig. 3b should be mainly composed of the LPSO phase, according to the composition analyses (Table 1). BSE-SEM observations indicated that the microstructure and phase constitution of sample S-573 (not shown here) are similar to that of sample S-473, which is consistent with the XRD analyses.

Fig. 3c shows typical microstructure of sample S-673. Numerous particles in white (an enlarged image shown as the inset of Fig. 3c), less than 1 μm, are embedded in the gray matrix, i.e. the LPSO phase, based on the EDX (Table 1) and XRD analyses (Fig. 2e). The composition of the white particles is different from that of white lamellae of sample S-cast or small particles of sample S-473 (Table 1), which

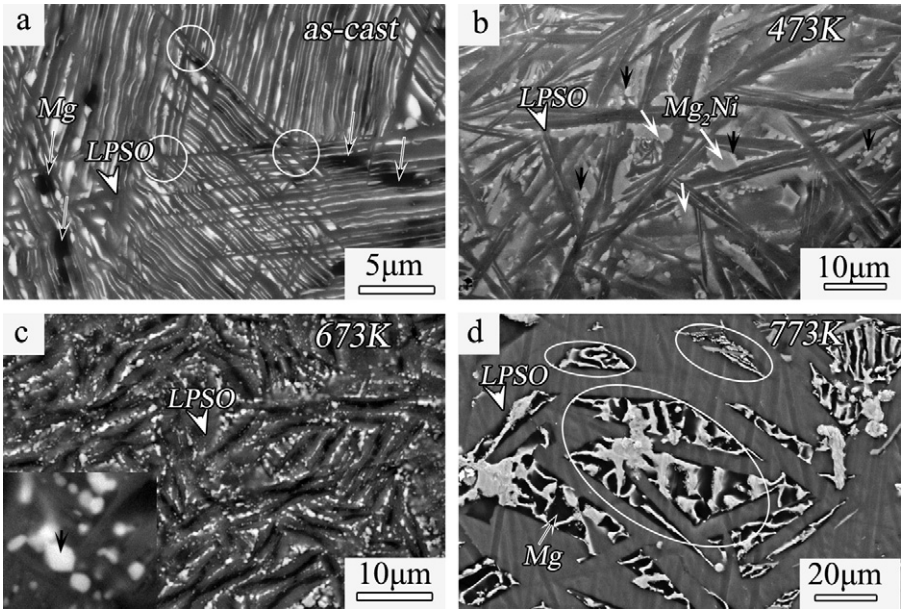

Fig. 3. BSE-SEM images of the Mg–Ni–Zn–Y alloy in different annealing states showing the evolution of the microstructures. (a) Sample S-cast; (b) Sample S-473 (473 K); (c) Sample S-673 (673 K) and (d) Sample S-773 (773 K), respectively.

Table 1
EDX analysis of various phases carried out in SEM on the Mg–Ni–Zn–Y alloy annealed at various temperatures.

Samples	Regions	Mg (at.%)	Ni (at.%)	Zn (at.%)	Y (at.%)
S-cast	Mg	93.1 ± 1.0	2.1 ± 0.9	1.1 ± 1.4	2.8 ± 1.2
	LPSO	88.7 ± 1.3	4.7 ± 0.8	1.4 ± 0.2	5.1 ± 0.6
	White lamellae	32.5 ± 2.7	29.8 ± 2.2	28.8 ± 1.9	8.9 ± 0.7
S-473	LPSO	88.1 ± 2.6	5.0 ± 1.4	1.0 ± 0.4	5.8 ± 1.5
	White particles	22.7 ± 3.3	30.6 ± 3.3	33.6 ± 2.0	13.1 ± 1.9
S-673	LPSO	88.8 ± 2.9	4.8 ± 1.7	1.0 ± 0.5	5.4 ± 1.4
	White particles	19.0 ± 1.1	34.4 ± 1.5	30.8 ± 1.9	15.7 ± 2.6
S-773	Mg	98.4 ± 2.5	0.7 ± 1.2	0.4 ± 0.4	0.6 ± 1.1
	LPSO	85.8 ± 2.1	5.4 ± 0.6	1.1 ± 0.3	7.7 ± 1.5

should correspond to the unidentified XRD peaks in spectrum (d) in Fig. 2. The microstructure characteristics of sample S-773 (Fig. 3d) changed dramatically from that of sample S-673 (Fig. 3c), although the phase constituents are similar according to the XRD results (spectra (d) and (e) in Fig. 2). Some large irregular mixture of white and black bands/blocks is embedded in the gray matrix, marked by ellipses in Fig. 3d. According to EDX analyses, the matrix and black bands are LPSO phase and Mg, respectively. The composition of white band/block is very close to that of small white particles in sample S-673 (Table 1), corresponding to the unidentified phase in sample S-773.

3.3. TEM characterization of the intermetallic phases

3.3.1. As-cast

Fig. 4a is a bright-field (BF) TEM image of sample S-cast, where two phases can be labeled according to the contrasting characteristics. Fig. 4b is a selected-area electron diffraction (SAED) pattern corresponding to the gray areas in Fig. 4a. In the SAED pattern, there are weaker spots at positions of $n/14\ (0002)_{Mg}$ (n is an integer), which indicates a 14H-LPSO phase known in several ternary Mg–Zn–RE alloys [8,15,16]. Fig. 4c is the atomic-resolution HAADF scanning-transmission electron microscopy (STEM) images of the 14H-LPSO phase, showing a stacking sequence of ABAB-CACACACBABA. And the ABCA-type stacking sequence is shown by color dots in Fig. 4c. The two brightest layers, in the mid-

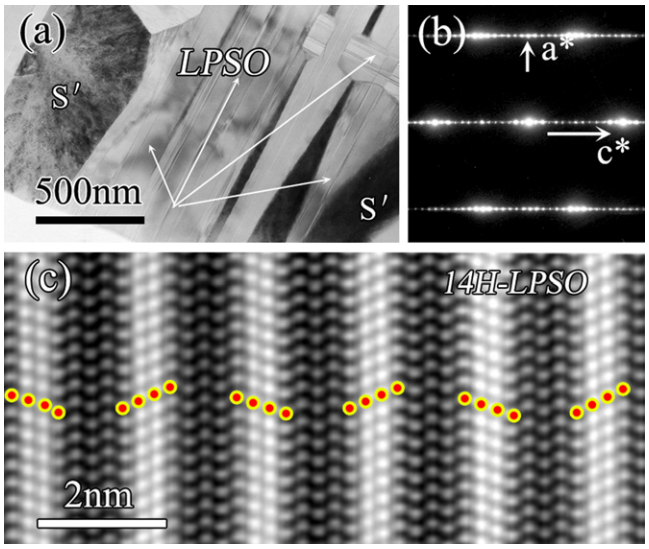

Fig. 4. (a) TEM image showing the morphology of the sample S-cast; (b) a SAED pattern of 14H-LPSO phase; and (c) Fourier-filtered HAADF-STEM image showing stacking sequence and the segregation layers of 14H-LPSO phase, and the ABCA-type stacking sequence is denoted by color dots in c.

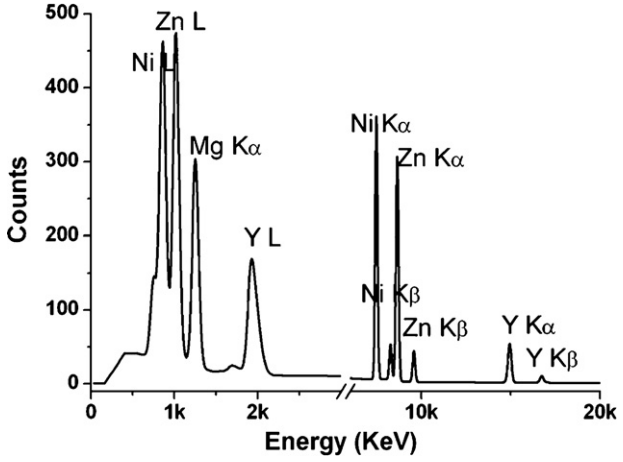

Fig. 5. Representative EDX spectrum recorded from the S′ phase denoted in Fig. 4, showing a high concentration of Zn and Ni in this phase.

dle of ABCA-type stacking sequence, must be rich of Y and/or Zn/Ni, since the spot intensity in the HAADF-STEM image is proportional to the square of atomic number [17]. Statistic analysis on 30 EDX spectra shows that the composition of the14H-LPSO phase is Mg:Ni:Zn:Y = (87.2 ± 0.7):(5.5 ± 0.5):(1.7 ± 0.1):(5.6 ± 0.4). This corresponds to the 14H-LPSO phase in Mg–Zn–Y alloy [14], if Ni in the present study is considered to substitute for some of Zn. Occasionally, we identified a small amount of 18R-LPSO phase in sample S-cast [18,19]. It is worthwhile to mention that the 14H-LPSO phase is predominant in the present Mg–Ni–Zn–Y cast alloy, while the 18R-LPSO phase is predominant in the ternary Mg–Zn–Y alloy [14,16,20]. Such a difference might be due to the addition of Ni and/or the different ratio of alloy elements.

Another phase labeled with 'S'' in Fig. 4a corresponds to the white lamella in the BSE-SEM micrograph shown in Fig. 3a. Fig. 5 shows an EDX spectrum from one S′ lamella. Statistic analysis on 30 such lamellae in different areas showed that the average composition of S′ phase was Mg:Ni:Zn:Y = (30.6 ± 1.5):(32.5 ± 1.0):(28.2 ± 1.1):(8.7 ± 0.4). It is seen that the concentration of Zn and Ni in S′ phase is higher than that in LPSO phase, which is consistent with the SEM measurements. In order to determine the crystal structure of the S′ phase, large-angle tilting electron diffraction experiments were carried out on several lamellae. Fig. 6 shows a series of SAED patterns obtained from a single S′ lamella. These SAED patterns cannot be indexed to any known binary (Mg–Ni or Mg–Zn) or ternary (Mg–Zn–Ni or Mg–Zn–Y) phases reported in the Mg–Ni–Zn–RE system. According to the geometric configuration of each pattern and the angles between any two patterns, a face-centered cubic (FCC) lattice can be identified. The experimental angle (without parentheses) between the two zone axis matches well with that of the calculated one (with parentheses). The $\{0\,2\,0\}_{S'}$ reflections are extinction in the [0 0 1] pattern, which indicates the presence of a diamond-type glide plane in this phase. Therefore, the possible space group is $Fd\bar{3}m$ and the lattice parameter is $a = 0.73$ nm. While those spots marked by white circles in the $[0\,1\,1]_{S'}$ zone axis pattern, corresponding to $\{0\,2\,0\}_{S'}$ and $\{2\,2\,\bar{2}\}_{S'}$ reflections, etc., which should be kinematically forbidden in the diamond-cubic structure, may arise from second diffraction. The peaks at 2θ of 40.78° and 42.72° in the XRD spectrum correspond respectively to $\{1\,1\,3\}_{S'}$ and $\{2\,2\,\bar{2}\}_{S'}$ reflections of the diamond-cubic phase found in the present Mg–Ni–Zn–Y alloy. This diamond-cubic quaternary phase is isotypic with Mg–Y–Ag ternary intermetallic phase [20].

The S′ phase features abundant nano-scaled regions within the lamellae, which can be classified into domains consisting of either thin laths or small disks, denoted by dotted ellipses and solid circles in Fig. 7a, respectively. The width of thin laths varies from 50 nm to 150 nm, while the diameter of disks is in the range of 10–50 nm. An SAED pattern from the regions marked with 'A' demonstrates that these laths are nano-twin bands. Fig. 7b is a $[1\,\bar{1}\,0]_{S'}$ HRTEM image of domain 'B' marked in Fig. 7a, showing the presence of microtwins and stacking faults (SFs), as indicated by white lines and arrows, respectively. Twins and/or SFs in various {1 1 1} planes intersect with each other, which are responsible for the Moire fringe shown by a circle in Fig. 7b.

3.3.2. Annealed

When the alloy is annealed at 473 K for 5 h, one of the salient features is the precipitation of hexagonal Mg_2Ni. Fig. 8a is a TEM micrograph showing the morphology of Mg_2Ni lath in sample S-473. Fig. 8b and c are SAED patterns, which can be indexed as $[1\,1\,\bar{2}\,0]$ and $[1\,0\,\bar{1}\,0]$ zone axes diffractions, respectively, of hexagonal Mg_2Ni phase with lattice parameters of $a = 0.5205$ nm and $c = 1.3236$ nm [21].

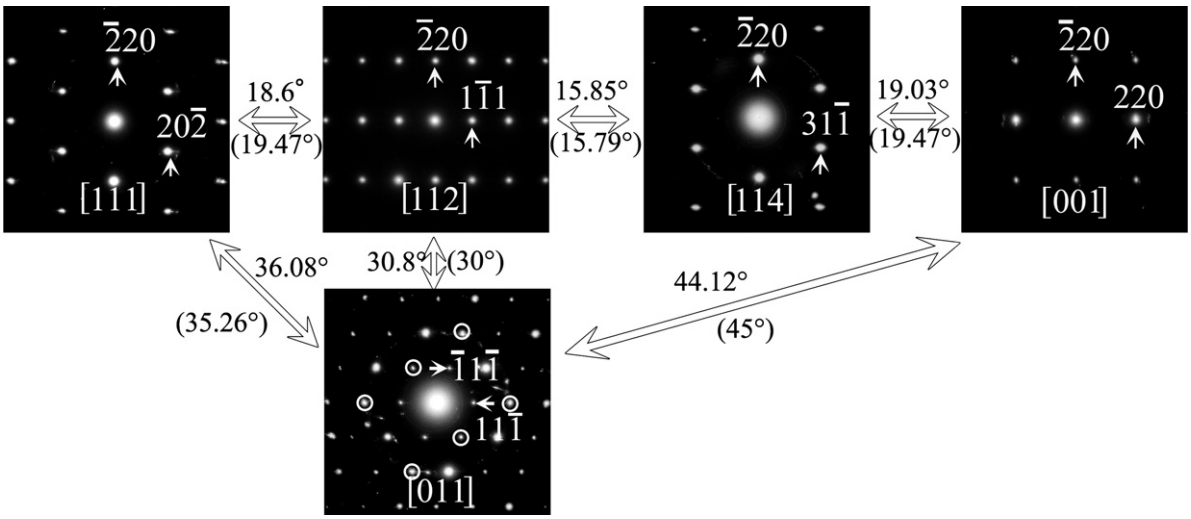

Fig. 6. A series of SAED patterns obtained from the S′ phase by large-angle tilting experiments. Angles without and with parentheses represent those of measured and calculated values between the zone axis. A diamond-cubic lattice can be identified based on the geometric configuration of patterns and the angles between any two patterns.

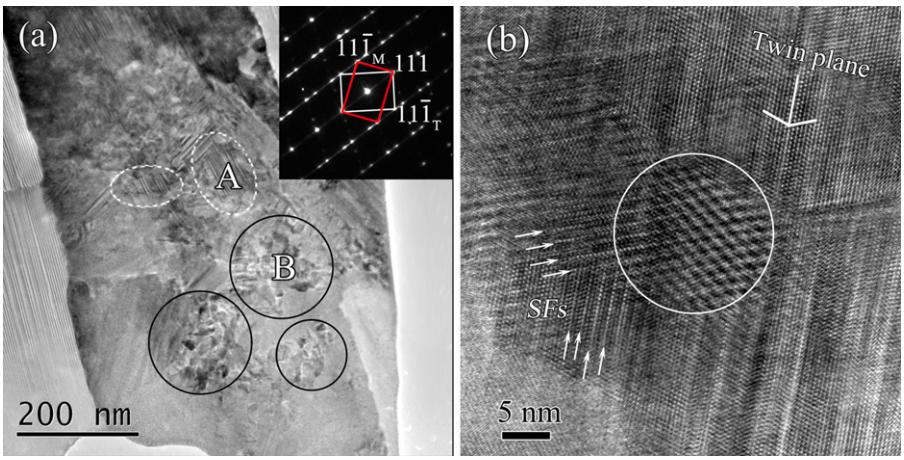

Fig. 7. (a) TEM image of S′ phase containing lot of nano-scale domains, denoted by either dotted ellipses or circles, the inset is an SAED pattern from the area marked by 'A'; (b) a typical HRTEM micrograph of the domain 'B' in $[1\ \bar{1}\ 0]_{S'}$ orientation revealing a nanotwin as indicated by white lines, and the arrows indicate SFs.

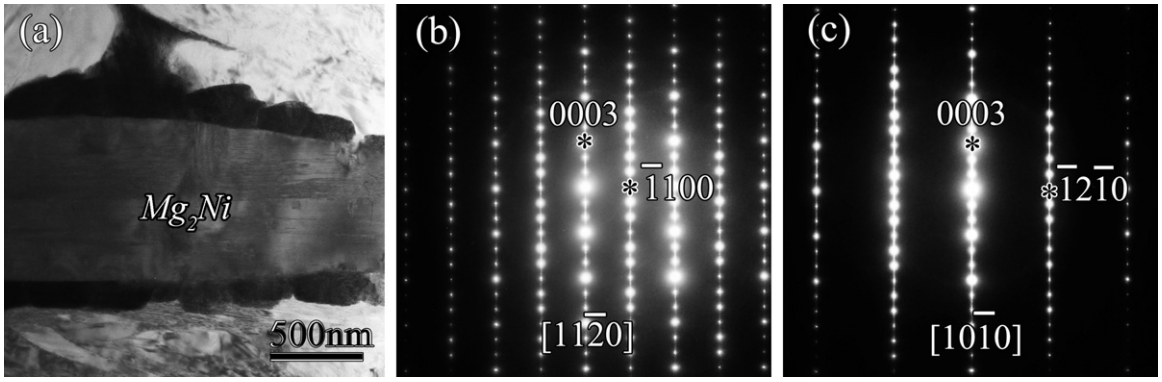

Fig. 8. (a) The microstructure of the Mg_2Ni phase in the sample S-473. (b) and (c) SAED patterns of Mg_2Ni recorded along $[1\ 1\ \bar{2}\ 0]$ and $[1\ 0\ \bar{1}\ 0]$ zone axis, respectively.

Fig. 9a shows a TEM image of the microstructure in the sample annealed at 773 K. An LPSO phase with 18R structure is identified by means of electron diffraction (Fig. 9b) and atomic resolution HAADF-STEM imaging (Fig. 9c). The angle between a^* and c^* reciprocal vectors is about 85.8°, smaller than 88° in Mg–1Zn–2Y (at.%) [6], and larger than 83.25° in Mg–8Y–2Zn–0.6Zr (wt.%) [20]. This might result from the substitution of Zn/Y by Ni in this LPSO phase. The stacking sequence of the present 18R-LPSO phase is the same as that of 18R-LPSO in Mg–Zn–Y ternary alloys [9,20]. It is worthwhile to mention that the 18R-LPSO phase is predominant in sample S-773, making a remarkable difference from that of the as-cast alloy where 14H type is the major LPSO structure. In other words, phase transformation from 14H to 18R-LPSO phase happens during annealing at 773 K in the present Mg–Ni–Zn–Y alloy. Such a transformation shows an opposite direction to that in Mg–Zn–Y alloys where 18R transforms to 14H-LPSO phase during annealing [16,20].

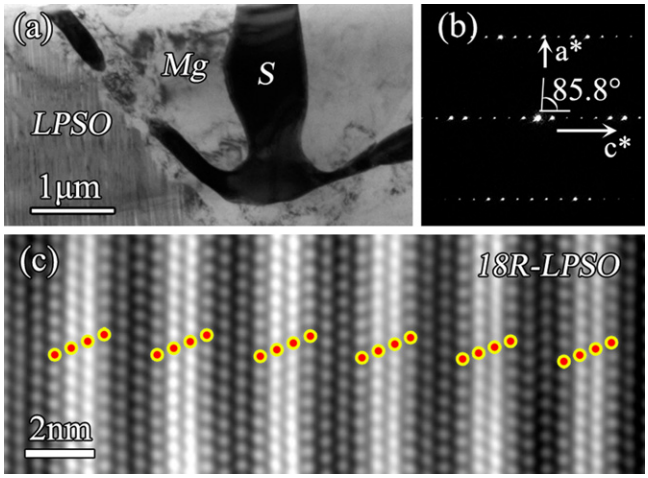

Fig. 9. (a)TEM image of sample S-773 showing the coexistence of Mg, S-phase and LPSO structure; (b) an SAED pattern of 18R-LPSO phase; (c) Fourier-filtered HAADF-STEM image showing stacking sequence and the segregation layers of 18R-LPSO phase, and the ABCA-type stacking sequence is denoted by color dots in c.

Fig. 10a is an EDX spectrum from the area labeled with 'S' in Fig. 9a, where atomic concentration of Mg/Ni/Zn/Y is approximately 18.5/36.8/31.1/13.6. Compared with compositions of S′ phase (Fig. 5), the concentration of Mg in this S phase is decreased by about 40%, while the content of Ni, Zn and Y is increased by about 13%, 10%, and 56%, respectively. Fig. 10b shows a series of SAED patterns of the S phase. A face-centered cubic structure can be identified, based on the configuration of each SAED pattern and the tilting angles between the two patterns. The lattice parameter is determined to be $a = 0.72$ nm and the space group of $Fm\bar{3}m$ is proposed based on the extinction rules. The remarkable increase in peak intensity at $2\theta = 67.33°$, and the corresponding reversion of peak intensity for the two peaks within the dashed rectangle in Fig. 2, in samples S-673 and S-773 is believed to result from the formation of S phase upon high temperature annealing, since {5 1 1} and/or {3 3 3} of S phase can be indexed for this peak according to Bragg formula. Therefore, based on the results of SAED patterns, the unidentified peaks of XRD patterns in Fig. 2 can be unambiguously explained by S′ and S phase at various states.

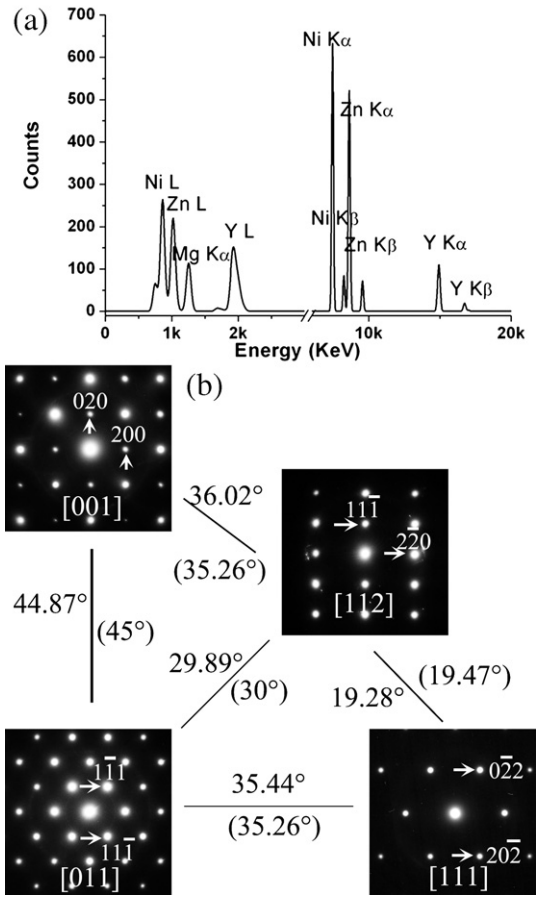

Fig. 10. (a) An EDX spectrum recorded from the black region of Fig. 9a, i.e. the S phase; (b) a series of SAED patterns obtained from the S phase by large-angle tilting experiments. An FCC lattice is deduced from the geometric configuration of patterns and the angles between any two patterns.

3.4. Phase transformation

It is seen in the above section that Mg_2Ni laths precipitated when the alloy was annealed at 473 K and 573 K. In most cases, S′ and S phases are found to coexist with the Mg_2Ni phase at these moderate annealing temperatures, as seen in Figs. 8a and 11a. The XRD peak splitting at $2\theta \approx 41^\circ$ ($40.78^\circ_{S'}$ and 41.30°_{S}) and $2\theta \approx 43^\circ$ ($42.72^\circ_{S'}$ and 43.14°_{S}) in Fig. 2 can be rationalized by the coexistence of the S′ and S phase. The boundary of S′/S is meandering. In addition, almost pure Mg-particles are present close to S′/S phases (arrowed in Fig. 11a). Taking into account the fact that the content of Mg significantly decreases from 31% in S′ phase to 18% in S phase, we propose that most of the Mg domains, adjacent to S′/S particles, result from the decomposition of the metastable S′ phase. The S phase and Mg_2Ni have a specific orientation relationship, according to the composite SAED patterns shown in Fig. 11b and c. That is $[1\,0\,\bar{1}\,0]_{Mg_2Ni}//[1\,1\,2]_S$, $[1\,1\,\bar{2}\,0]_{Mg_2Ni}//[0\,1\,1]_S$ and $(0\,0\,0\,1)_{Mg_2Ni}//(1\,1\,\bar{1})_S$. Moreover, Mg_2Ni and S phase share a coherent interface (Fig. 11d), since $d_{\{0\,0\,0\,3\}Mg_2Ni} \approx d_{\{1\,1\,1\}S}$ and $d_{\{1\,1\,\bar{2}\,0\}Mg_2Ni} \approx d_{\{2\,2\,0\}S}$.

The microstructures in the samples which suffered high temperature annealing changed distinctly. Fig. 12 shows a low magnification STEM image of sample S-673. The S phase, LPSO phase and Mg, confirmed by SAED patterns and nano-probe EDX analysis, exhibit white, bright gray and dark gray contrast. The S particles with 100–500 nm in diameter, are enveloped by Mg grains, such a mixture sandwiching within the LPSO matrix. A small amount of isolated S′ phase was identified, but Mg_2Ni phase was not detected in sample S-673. This means that the S phase gradually takes the place of the S′ and Mg_2Ni phases during annealing. When annealing temperature increases to 773 K, the S phase, LPSO phase and Mg grains apparently grow, forming the coarse-grained microstructure shown in Figs. 3d and 9a.

Based on the above experimental observations, we summarize the phase evolution of $Mg_{83}Ni_6Zn_5Y_6$ alloy during annealing in Table 2, and propose the following procedures of phase transformation:

$$S' + 14H \overset{473\,K/573\,K}{\longrightarrow} S' + Mg_2Ni + S + 14H \overset{673\,K/773\,K}{\longrightarrow} S + Mg + 18R.$$

Here, the Mg_2Ni phase first precipitated in the sample annealed at 473 K, but it decomposed when the sample was annealed at 673 K. Therefore, the Mg_2Ni is a transition phase, which may play a critical role in phase transformation from the S′ phase to the S phase.

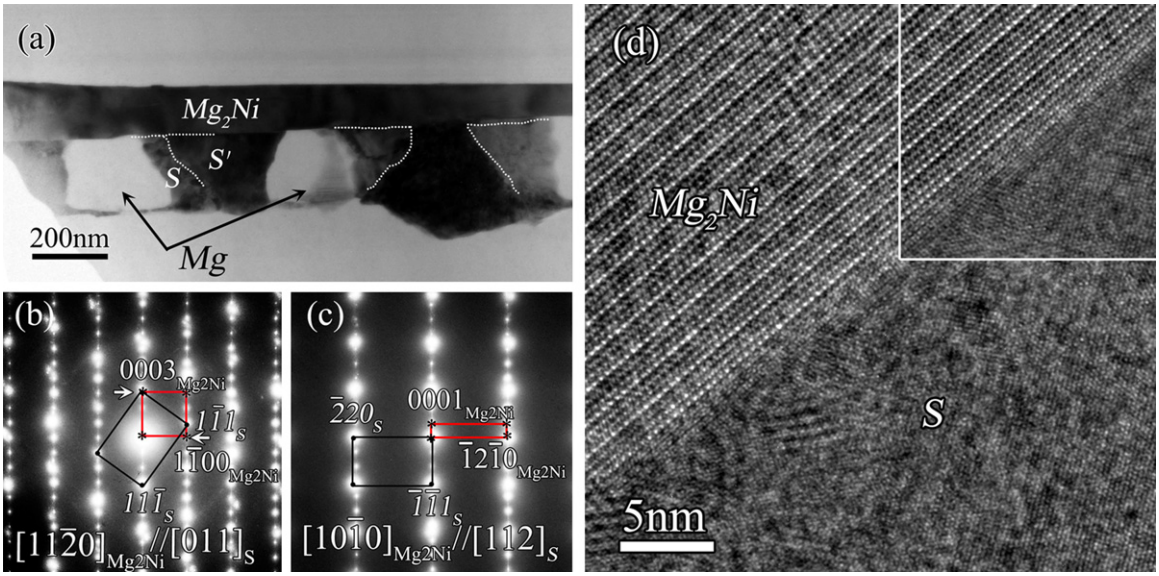

Fig. 11. (a) The microstructure of Mg_2Ni and S′/S phase in the sample S-473. The dashed lines show the boundaries of the Mg_2Ni phase, S′ and S phase, and the arrows denoted the Mg existing between particles; (b) and (c) compositive SAED patterns from Mg_2Ni phase and S phase, recorded along $[1\,0\,\bar{1}\,0]_{Mg_2Ni}$ and $[1\,1\,\bar{2}\,0]_{Mg_2Ni}$, respectively; (d) HRTEM image of the coherent interface between Mg_2Ni and S phase, the Wiener filtered image inset in the up right corner.

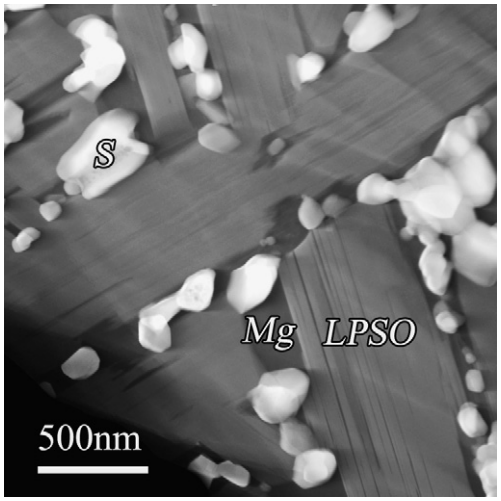

Fig. 12. Low magnification STEM image showing the microstructure of the sample S-673. The S phase, Mg and LPSO phase exhibit white, dark gray and bright gray contrast, respectively.

4. Discussion

It is known that the LPSO phase [5–7,22], eutectic phase, and refinement of Mg dendrites [12] play critical roles and make Mg alloys exhibit superior mechanical performance. In the present $Mg_{83}Ni_6Zn_5Y_6$ alloy with as-cast state, the microstructure features a combination of LPSO thin lamellae and S′ phase. This is different from the quaternary $Mg_{90}(Cu_{0.667}Y_{0.333})_4Zn_6$ system which is composed of Mg, Cu_2Mg and CuZnMg [12]. Although the microhardness of the present $Mg_{83}Ni_6Zn_5Y_6$ cast alloy (116.2 ± 13.7) is similar to that of the Mg–Zn–Y alloy containing the LPSO phase (about 112) [9] and that of AZ91D reinforced by SiC particles (about 120) [23], it is much higher than ordinary Mg alloys (about 60–80) [24–26] and pure Mg (about 40–50) [27,28]. The high value of microhardness in the present alloy is believed to result from the higher fraction of the LPSO phase, layered composite microstructure of the LPSO phase and the S′ phase.

The microhardness of samples S-473 and S-573, 134.8 ± 10.2 and 147.6 ± 11.2, exhibits an increase of 15% and 27%, respectively, compared to sample S-cast (116.2 ± 13.7). Such an increase results from the co-precipitation of Mg_2Ni and S phases. In addition, the coherent interface between Mg_2Ni/S phases and consequently their orientation relationship plays a critical role. This orientation relationship between Mg_2Ni and S phase were retained when annealing temperature up to 573 K and the microhardness remained higher at this annealing temperature.

The drop of microhardness of sample S-673 results from the dissolution of Mg_2Ni precipitates and the loss of S/Mg_2Ni coherent interface. Namely, the effects of precipitation strengthening and coherent interface strengthening on the microhardness were quickly lowered with increasing the annealing temperature above 573 K.

Table 2
Phase evolution of the $Mg_{83}Ni_6Zn_5Y_6$ alloy during annealing.

Heat treatment condition	$Mg_{83}Ni_6Zn_5Y_6$
As cast	14H[a], S′ ($Fd\bar{3}m$, $a = 0.73$ nm)
473 K, 5 h	14H[a], S′, S ($Fm\bar{3}m$, $a = 0.72$ nm), Mg_2Ni
573 K, 5 h	14H[a], S′, S, Mg_2Ni
673 K, 5 h	18R[b], S′, S, Mg
773 K, 5 h	18R[b], S, Mg

[a] Most of LPSO phases are 14H-LPSO, and a small amount are 18R-LPSO.
[b] Most of LPSO phases are 18R-LPSO, and a small amount are 14H-LPSO.

In addition to Mg grains, 18R-LPSO phase and S phase are the major phases in the alloy annealed at 773 K for 5 h. However, the grain size of all these phases is much coarser (Figs. 3d and 9a). We calculated the weighted average microhardness (105.9 ± 4.7) for sample S-773 according to $H = H_{LPSO}f_{LPSO} + H_{mixture}f_{mixture}$. Here H and f represent the microhardness and fraction of a specific phase or a mixture with some phase components. The microhardnesses were 97.7 ± 5.0 for 18R-LPSO phase and 121.3 ± 4.5 for regions consisting of the Mg and S phase. And their volume fractions were measured as 65.2% and 34.8%, respectively, based on statistics of SEM images. It is of interest to note that the microhardness of the 18R-LPSO phase in sample S-773 is approximately equal to that in sample S-673, which implies that the microhardness of the sample S-673 is mostly contributed by the LPSO matrix. And the S phase must be harder than the LPSO phase, since Mg is softer than the LPSO phase [9,14] but a combination of S phase and Mg (121.3 ± 4.5) is harder than the LPSO phase (97.7 ± 5.0). Thus the LPSO phase and a mixture of Mg and S phase contribute to a higher microhardness of Mg–Ni–Zn–Y alloy than ordinary Mg alloys [24–26] even after grain coarsening.

5. Concluding remarks

We have carried out a detailed study on microstructure and microhardness evolution in a $Mg_{83}Ni_6Zn_5Y_6$ alloy during annealing. We conclude the following remarks:

(1) The as-cast $Mg_{83}Ni_6Zn_5Y_6$ (at.%) alloy is composed of Mg, 14H-LPSO phase, and a diamond-cubic quaternary metastable phase (S′) with possible space group of $Fd\bar{3}m$ and lattice parameter of $a = 0.73$ nm. Multiple microtwins and highly dense stacking faults are the salient features in the S′ phase.
(2) Mg_2Ni laths and a nanometer-sized S phase ($Fm\bar{3}m$, $a = 0.72$ nm) co-precipitated on the consumption of the S′ phase upon annealing at 473 K and 573 K. After annealing at higher temperatures, the Mg_2Ni and S′ phase transformed to the S phase, and the 14H-LPSO phase was replaced by the 18R-LPSO phase.
(3) The relatively high microhardness of the as-cast alloy results from harder LPSO phase and grain refinement strengthening. When the alloy is annealed at moderate temperatures range from 473 to 573 K, the precipitation of Mg_2Ni laths and S particles result in a significant increase of microhardness owing to precipitate strengthening and coherent interface (S/Mg_2Ni) strengthening. High temperature annealing over 573 K causes a drop in microhardness, since at this stage the Mg_2Ni precipitates were dissolved and consequently the coherent S/Mg_2Ni interface vanished.

Acknowledgements

This work is supported by the National Natural Science Foundation of China and National Basic Research Program of China (2009CB623705).

References

[1] B. Mordike, Mater. Sci. Eng. A 324 (2002) 103–112.
[2] A. Singh, M. Nakamura, M. Wantanabe, A. Kato, A.P. Tsai, Scr. Mater. 49 (2003) 417–422.
[3] D.H. Bae, S.H. Kim, D.H. Kim, W.T. Kim, Acta Mater. 50 (2002) 2343–2356.
[4] J. Lee, D. Kim, H. Lim, Mater. Lett. 59 (2005) 3801–3805.
[5] A. Inoue, Y. Kawamura, M. Matsushita, K. Hayashi, J. Koike, J. Mater. Res. 16 (2001) 1894–1900.
[6] E. Abe, Y. Kawamura, K. Hayashi, A. Inoue, Acta Mater. 50 (2002) 3845–3857.
[7] Y. Kawamura, T. Kasahara, S. Izumi, M. Yamasaki, Scr. Mater. 55 (2006) 453–456.
[8] S. Yoshimoto, M. Yamasaki, Y. Kawamura, Mater. Trans. 47 (2006) 959–965.
[9] X.H. Shao, Z.Q. Yang, X.L. Ma, Acta Mater. 58 (2010) 4760–4771.
[10] T. Itoi, K. Takahashi, H. Moriyama, M. Hirohashi, Scr. Mater. 59 (2008) 1155–1158.

[11] T. Spassov, P. Solsona, S. Surinach, M. Baro, J. Alloys Compd. 345 (2002) 123–129.
[12] C. Zhang, X. Hui, K. Yao, Z. Li, G. Chen, Mater. Sci. Eng. A 491 (2008) 470–475.
[13] D.H. Ping, K. Hono, Y. Kawamura, A. Inoue, Philos. Mag. Lett. 82 (2002) 543–551.
[14] T. Itoi, T. Seimiya, Y. Kawamura, M. Hirohashi, Scr. Mater. 51 (2004) 107–111.
[15] M. Matsuda, S. Ii, Y. Kawamura, Y. Ikuhara, M. Nishida, Mater. Sci. Eng. A 393 (2005) 269–274.
[16] Y. Kawamura, M. Yamasaki, Mater. Trans. 48 (2007) 2986–2992.
[17] S. Pennycook, D. Jesson, Acta Metall. Mater. 40 (1992) S149–S159.
[18] Z. Luo, S. Zhang, Y. Tang, D. Zhao, J. Mater. Sci. Lett. 209 (1994) 275–278.
[19] Z. Luo, S. Zhang, J. Mater. Sci. Lett. 19 (2000) 813–815.
[20] Y. Zhu, A. Morton, J. Nie, Acta Mater. 58 (2010) 2936–2947.
[21] J. Soubeyroux, D. Fruchart, A. Mikou, M. Pezat, B. Darriet, Mater. Res. Bull. 19 (1984) 895–904.
[22] D. Li, X. Zeng, J. Dong, C. Zhai, W. Ding, J. Alloys Compd. 468 (2009) 164–169.
[23] J. Lan, Y. Yang, X. Li, Mater. Sci. Eng. A 386 (2004) 284–290.
[24] Y. Lü, Q. Wang, X. Zeng, W. Ding, C. Zhai, Y. Zhu, Mater. Sci. Eng. A 278 (1999) 66–76.
[25] W. Kim, S. Hong, Y. Kim, S. Min, H. Jeong, J. Lee, Acta Mater. 51 (2003) 3293–3307.
[26] Y.X. Wang, S.K. Guan, X.Q. Zeng, W.J. Dine, Mater. Sci. Eng. A 416 (2006) 109–118.
[27] R. Saravanan, M. Surappa, Mater. Sci. Eng. A 276 (2000) 108–116.
[28] S.F. Hassan, M. Gupta, Mater. Sci. Eng. A 392 (2005) 163–168.